

Dissipative acousto-mechanical parametric interface between high-overtone acoustics and flexural phonons

Xun Ji,^{1,2,3,*} Huanying Sun,^{1,*} Longhao Wu,⁴ Qichun Liu,¹ Yulong Liu,^{1,†} Mika A. Sillanpää,⁴ and Tiefu Li^{5,1,‡}

¹*Beijing Key Laboratory of Fault-Tolerant Quantum Computing,
Beijing Academy of Quantum Information Sciences, Beijing 100193, China*

²*Beijing National Laboratory for Condensed Matter Physics,
Institute of Physics, Chinese Academy of Sciences, Beijing 100190, China*

³*University of Chinese Academy of Sciences, Beijing 100049, China*

⁴*Department of Applied Physics, Aalto University, FI-00076 Aalto, Finland*

⁵*School of Integrated Circuits, BNRist and Frontier Science Center for Quantum Information, Tsinghua University, Beijing 100084, China*

(Dated: May 26, 2026)

High-overtone bulk acoustic wave resonators (HBARs) promise advanced phononics, yet achieving non-linearity remains challenging. We demonstrate a radiation-pressure-type parametric interaction between GHz HBARs and low-frequency flexural modes in a suspended silicon nitride membrane, where mechanical displacement modulates the external dissipation rate to enable dissipative acousto-mechanical coupling. Benefiting from the high quality factor, the system enters the resolved-sideband regime at room temperature, yielding acousto-mechanically induced transparency. We observe tunable Kerr nonlinearity and generate coherent HBAR frequency combs via two-tone driving. Notably, our dissipative coupling strength is 20 times larger than the dispersive coupling, the highest ratio among reported hybrid dissipative-dispersive coupling systems, resulting in the experimental observation of amplification in the reflection spectra under red-sideband driving. The ability to interface dense HBAR modes with a common mechanical resonator provides a scalable on-chip platform for multimode phononic information processing, with quantum phononics potentially achievable at sub-Kelvin temperatures.

High-overtone bulk acoustic resonators (HBARs) serve as versatile platforms by supporting high-order harmonics within macroscopic substrates. Their capacity for exceptionally high frequency-quality factor product ($f \times Q$) at gigahertz (GHz) frequencies has spurred widespread adoption across advanced phononic applications [1–4]. Recently, HBARs have emerged as a cornerstone in quantum acoustodynamics, owing to their demonstrated capability for phononic quantum information processing [5–9]. In the microwave frequency band, the piezoelectric effect enables strong coupling between HBARs and superconducting resonators, with interaction strengths reaching the megahertz (MHz) regime [10, 11]. Leveraging this electric-dipole-like coupling, strong interactions with superconducting qubits at the single-phonon level have been realized [12–18], enabling deterministic preparation of non-Gaussian phononic states [19, 20], among others. In the optical domain, parametric coupling between HBARs and optical cavities has been explored through photoelastic effect [21–25], with recent demonstrations showing that HBAR-microring integration facilitates electro-optic modulation [26–29]. These systems have demonstrated the microwave-to-optical transduction efficiency approaches 1% and is fundamentally limited by the electro-optic coefficients [30–32].

Concurrently, two-dimensional (2D) membrane mechanical resonators, typically operating in the sub-MHz range, have emerged as pivotal components in quantum phononics [33–39]. In the optical domain, low-loss silicon nitride (SiN) membranes are widely employed in high- Q optical microcavities [40–43] to explore optomechanical modulation. Notably, by integrating bandgap-engineered SiN membranes within high-finesse Fabry-Pérot cavities, quantum control of mechanical motion has been achieved [44–46]. Despite this

progress, the substantial frequency mismatch between these low-frequency 2D flexural modes and superconducting qubits poses a significant barrier to direct interaction in the GHz band [47–49]. While flexural 2D membrane resonators offer superior parametric coupling to optical fields, and bulk acoustic waves (BAWs) provide ideal resonant frequencies for microwave qubit interfacing, a hybrid platform that bridges the advantages of both remains elusive [50–56]. This gap stems from the formidable challenge of engineering efficient parametric interactions between phononic modes across such disparate frequency regimes.

In this work, we demonstrate a hybrid acousto-mechanical interface that enables parametric coupling between HBARs and low-frequency SiN membrane resonators. Our design features a readout electrode patterned directly on the suspended membrane, which translates mechanical displacement into modulation of the HBAR’s external dissipation rate, κ_{ex} , thereby realizing a dissipative optomechanical-like coupling [57–65]. This approach overcomes the long-standing challenge of achieving sizable dissipative coupling in integrated electromechanical systems. Moreover, it achieves operation in the resolved-sideband regime at room temperature, unlike conventional superconducting electromechanical systems that require cryogenic conditions. Experimentally, we observe acousto-mechanically induced transparency (AMIT) under low-power pumping. With high-power red-sideband pumping, we demonstrate amplification in the reflection spectrum. Furthermore, leveraging the intrinsic Kerr nonlinearity enables the generation of phase-coherent acoustic frequency combs (AFCs). This versatile on-chip architecture, capable of interfacing a vast manifold of HBAR modes with a common mechanical resonator, provides a scalable framework for

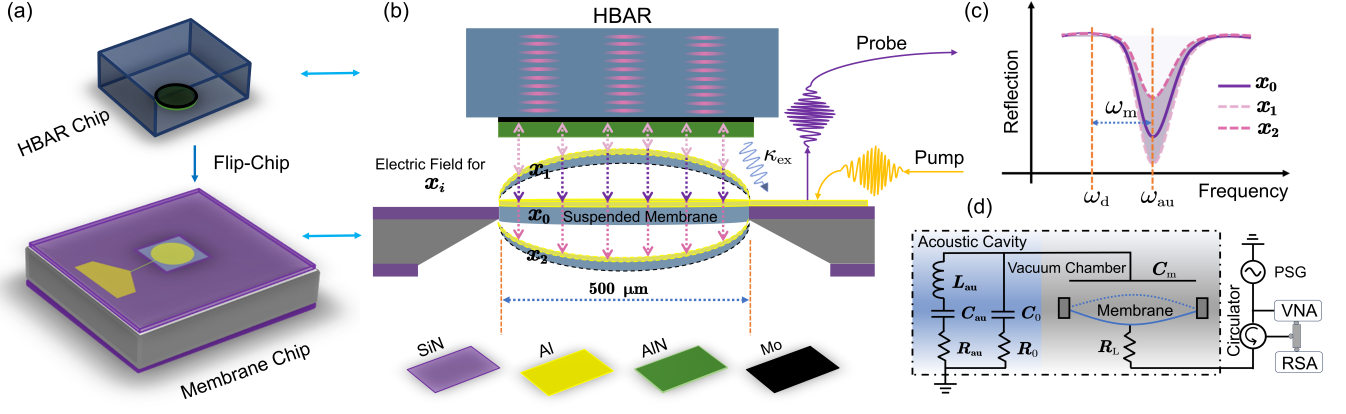


FIG. 1. (a) Schematic of the dissipative acousto-mechanical interface (not to scale), featuring a high-overtone bulk acoustic resonator (HBAR) and a SiN membrane mechanical resonator integrated via flip-chip bonding. (b) Conceptual illustration of the coupling: the flexural displacement of the membrane modulates the HBAR’s external dissipation rate κ_{ex} . (c) Schematic of the probed reflection spectra $|S_{11}|$ for varying membrane displacements x_i ($x_0 < x_1 < x_2$). The varying attenuation directly manifests the dissipative coupling. (d) Equivalent lumped-element circuit and experimental configuration. All measurements are conducted at room temperature in a high-vacuum chamber. PSG: multi-channel phase-coherent signal generator; VNA: vector network analyzer; RSA: real-time spectrum analyzer.

exploring many-body phonons.

Dissipative acousto-mechanical interface.—As illustrated in Fig. 1(a), our device features a hybrid flip-chip architecture that integrates a high-frequency HBAR with a low-frequency flexural SiN membrane resonator. To facilitate the acousto-mechanical interaction, the HBAR is accessed via a metallized SiN membrane that is held at a sub-micron distance in a flip-chip scheme. The HBAR is fabricated on a 250- μm -thick sapphire substrate, comprising a 60-nm-thick molybdenum (Mo) bottom electrode and a 1- μm -thick aluminum nitride (AlN) piezoelectric layer deposited via sequential sputtering. The mechanical resonator consists of a 50-nm-thick low-loss SiN membrane, grown via low-pressure chemical vapor deposition (LPCVD) on a silicon substrate. At the center of the SiN chip, a 500 $\mu\text{m} \times 500 \mu\text{m}$ suspended window is coated with a 20-nm-thick aluminum (Al) layer. The metallization extends to an external coupler port of the HBAR, thus serving as a functional electrode that translates mechanical flexural motion into modulation of the HBAR’s external coupling.

The side view of the flip-chip assembly is depicted in Fig. 1(b). The AlN layer serves as a high-efficiency electromechanical transducer, exciting a dense spectrum of longitudinal HBAR modes within the sapphire substrate. This substrate acts as a high- Q acoustic Fabry–Pérot cavity, where the longitudinal modes are confined between the AlN/Mo interface and the sapphire/air boundary. The fundamental interaction mechanism hinges on the sensitive modulation of the acoustic cavity’s external dissipation rate, κ_{ex} , by the out-of-plane displacement x of the SiN membrane. As shown in Fig. 1(c), each membrane displacement x_i leads to a different external coupling strength, manifesting as a controllable contrast in the microwave reflection $|S_{11}|$ spectra.

To quantitatively describe the hybrid system, we employ the modified Butterworth-Van Dyke (MBVD) lumped-element

model [8], as depicted in Fig. 1(d). Each HBAR overtone is represented by a motional branch consisting of a series $L_{\text{au}}\text{-}C_{\text{au}}\text{-}R_{\text{au}}$ circuit. The SiN membrane electrode and the Mo layer form a parallel-plate structure with a displacement-dependent capacitance $C_m(x)$, which shunts the HBAR motional branches. The total device impedance is given by:

$$Z = R_L + \frac{1}{j\omega C_m} + (Z_{\text{au}} \parallel Z_0). \quad (1)$$

Here, $Z_{\text{au}} = R_{\text{au}} + j\omega L_{\text{au}} + 1/(j\omega C_{\text{au}})$ is the characteristic impedance of the acoustic mode, $Z_0 = R_0 + 1/(j\omega C_0)$ represents the dielectric loss of piezoelectric materials, and the external load $Z_m = R_L + 1/(j\omega C_m)$ is modulated by the mechanical mode. In our electromechanical system, the membrane displacement modulates both the resonance frequency and the external dissipation rate of the HBAR. The respective single-photon coupling strengths are defined as $g_{\text{disp}} = -\frac{\partial\omega}{\partial x} x_{\text{zpf}}$ and $g_{\text{diss}} = \frac{\partial\kappa_{\text{ex}}}{\partial x} x_{\text{zpf}}$, where x_{zpf} is the zero-point fluctuation of the SiN flexural mode. Under the resonance frequency approximation $\omega_{\text{au}} = 1/\sqrt{L_{\text{au}}C_{\text{au}}}$, analysis of the lumped-element network yields the ratio of the single-photon dispersive to dissipative coupling strengths $|\frac{g_{\text{disp}}}{g_{\text{diss}}}| = \frac{1}{2\beta(2-\eta)}$, where $\beta = \omega_{\text{au}}R_L C_m$ and $\eta = C_m/(C_0 + C_m)$. Indeed, the static capacitance C_0 is much larger than the coupling capacitance C_m ($\eta \ll 1$). Hence, when $\beta > 1/4$, dissipative coupling dominates, and consequently $|g_{\text{diss}}| > |g_{\text{disp}}|$. In this regime, the dissipative coupling strength simplifies to $g_{\text{diss}} = 2\omega_{\text{au}}^2 R_L \frac{C_m}{C_0} \frac{dC_m}{dx} x_{\text{zpf}}$. As these relations indicate, increasing the coupling capacitor C_m directly enhances the relative strength of dissipative coupling (see Supplemental Material [66]). The equivalent circuit model gives preliminary single-photon dissipative and dispersive couplings. The acousto-mechanical coupling model further clarifies their effective coupling contributions.

We consider the interaction between this specific HBAR longitudinal mode centered at ω_{au} and the fundamental flexural mode of the SiN membrane at ω_{m} . The single-mode description is legitimate, as the energy scales related to the mechanics and the interaction are much smaller than the free spectral range (FSR). To coherently control the interaction, the HBAR mode is driven by a strong microwave pump at frequency ω_{d} , with a detuning $\Delta \equiv \omega_{\text{d}} - \omega_{\text{au}}$. A weak coherent probe tone with strength Ω_{p} at frequency ω_{p} is simultaneously applied to the system. The dynamics are governed by the system-bath interaction Hamiltonian [57, 66]. In the rotating frame of the pump frequency ω_{d} , the linearized equations of motion are obtained as:

$$\begin{aligned} \dot{\hat{d}} &= -(iG_{\text{disp}} + G_{\text{diss}})(\hat{c} + \hat{c}^\dagger) + (i\Delta - \frac{\kappa}{2})\hat{d} \\ &\quad - \sqrt{\kappa}\hat{a}_{\text{in}} - i\Omega_{\text{p}}e^{i(\omega_{\text{d}} - \omega_{\text{p}})t}, \\ \dot{\hat{c}} &= -iG_{\text{disp}}(\hat{d} + \hat{d}^\dagger) + G_{\text{diss}}(\alpha^*\hat{\xi}_{\text{in}} + \hat{d}^\dagger - \hat{d} - \alpha\hat{\xi}_{\text{in}}^\dagger) \\ &\quad - (i\omega_{\text{m}} + \frac{\gamma_{\text{m}}}{2})\hat{c} - \sqrt{\gamma_{\text{m}}}\hat{c}_{\text{in}}. \end{aligned} \quad (2)$$

Here, \hat{d} (\hat{d}^\dagger) and \hat{c} (\hat{c}^\dagger) are the annihilation (creation) operators for the fluctuations of cavity mode \hat{a} and mechanical mode \hat{b} , introduced via the standard linearization $\hat{a} = \bar{a} + \hat{d}$ and $\hat{b} = \bar{b} + \hat{c}$. The mechanical damping rate is γ_{m} . The total damping rate of the HBAR mode is $\kappa = \kappa_{\text{in}} + \kappa_{\text{ex}}$, where κ_{in} is the internal dissipation rate and $\kappa_{\text{ex}} = \kappa_{\text{c}} + g_{\text{diss}}(\bar{b} + \bar{b}^\dagger)$ is the external dissipation rate modified by external coupling. κ_{c} denotes the external coupling strength in the absence of any pump injection. Vacuum input noise through the drive port is denoted $\hat{\xi}_{\text{in}}$. The steady-state intracavity field \bar{a} is related to the classical input amplitude \bar{a}_{in} by $\bar{a} = \alpha\bar{a}_{\text{in}}$, with the cavity response coefficient given by $\alpha \approx \sqrt{\kappa_{\text{c}}}/(\kappa/2 - i\Delta)$. The enhanced dispersive and dissipative coupling rates are $G_{\text{disp}} = g_{\text{disp}}\bar{a}$ and $G_{\text{diss}} = g_{\text{diss}}(-\frac{i\Delta}{2\kappa_{\text{c}}} + \frac{\kappa_{\text{in}}}{4\kappa_{\text{c}}} + \frac{1}{4})\bar{a}$, respectively. In the cavity equation of motion, the mechanical displacement $\hat{c} + \hat{c}^\dagger$ couples to the cavity fluctuation via the complex coefficient $iG_{\text{disp}} + G_{\text{diss}}$. In the mechanical equation, the dissipative coupling additionally contributes a direct backaction term. In the resolved-sideband regime, G_{diss} is enhanced by a factor of $\Delta/\kappa_{\text{c}} \approx 8$ in our system. Together with the intrinsic condition $|g_{\text{disp}}/g_{\text{diss}}| < 1$, this leads to $|G_{\text{disp}}| \ll |G_{\text{diss}}|$, demonstrating the dominance of dissipative coupling.

In our experiments, all measurements were conducted in a high-vacuum chamber at room temperature. The microwave reflection spectrum, presented in Fig. 2(a), reveals a dense manifold of high-order longitudinal acoustic modes within the 2.5–4 GHz window. The measured FSR of $\mathcal{F}_0/2\pi \approx 21.37$ MHz matches the ballistic phonon model $\mathcal{F}_0 = v/2d$, where $v \approx 1.04 \times 10^4$ m/s is the longitudinal velocity in the sapphire substrate with thickness $d = 250$ μm . In this high- Q regime, the modal linewidths are governed by the interplay between intrinsic Akhiezer-type phonon scattering [67, 68] and surface boundary scattering, the latter becoming increasingly dominant as the phonon wavelength approaches the inter-

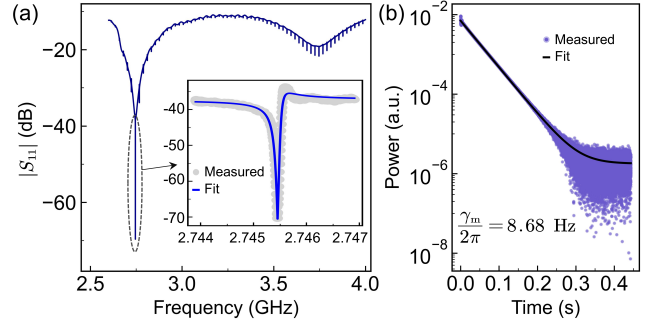


FIG. 2. (a) Microwave reflection spectra $|S_{11}|$ of selected HBAR modes. The inset shows a zoomed-in view of an acoustic mode along with its Lorentzian fit. (b) Ringdown measurement of the fundamental flexural mechanical mode of the SiN membrane.

face roughness at higher frequencies (see Supplemental Material [66]). Specifically, we focus on a representative resonance at $\omega_{\text{au}}/2\pi = 2.7454$ GHz, which exhibits a total quality factor of $Q \approx 1.89 \times 10^4$. This mode operates in the critical coupling regime ($\kappa_{\text{ex}} \approx \kappa_{\text{in}}$), with an external coupling rate $\kappa_{\text{ex}}/2\pi = 72.93$ kHz and an intrinsic dissipation rate $\kappa_{\text{in}}/2\pi = 72.5$ kHz.

The out-of-plane fundamental flexural mode of the SiN membrane with resonance frequency $\omega_{\text{m}}/2\pi = 571.5$ kHz was characterized using VNA and RSA. By applying a red-detuned pump ($\Delta \approx -\omega_{\text{m}}$) and a resonant probe, we tracked the energy decay through the evolution of the in-phase and quadrature (IQ) components, as shown in Fig. 2(b). To minimize backaction-induced linewidth broadening and ensure the measurement reflects the intrinsic dissipation, these ringdowns were performed in the low-power limit. The time-domain ringdown of the quadrature components yields a relaxation time of $\tau = 36.7$ ms, from which the intrinsic mechanical damping rate is extracted as $\gamma_{\text{m}}/2\pi = 8.68 \pm 0.2$ Hz. Furthermore, the single-photon acousto-mechanical coupling strength is determined to be $g_0/2\pi = 0.059$ Hz (see Supplemental Material [66]). Next, using the same pump and probe setup, we also analyzed the effective coupling of the system.

Acousto-mechanically induced transparency.—In the resolved-sideband regime ($\omega_{\text{m}} > \kappa$), a strong red-detuned drive enables coherent control of the flexural mechanical mode via the HBAR acoustic field. When a weak probe sweeps across the resonance and its detuning from the drive equals ω_{m} , coherent oscillations of the membrane generate Stokes and anti-Stokes sidebands. The destructive interference between the anti-Stokes field and the probe field manifests as a narrow transparency window in the acoustic reflection spectrum. This phenomenon, termed acousto-mechanically induced transparency (AMIT), signifies the suppression of probe absorption via a mechanically mediated destructive pathway. With the red-detuning anchored at $\Delta = -\omega_{\text{m}}$ and accounting for both acoustic and mechanical dissipation, the effective probe transmission spectrum $t_p(\delta)$

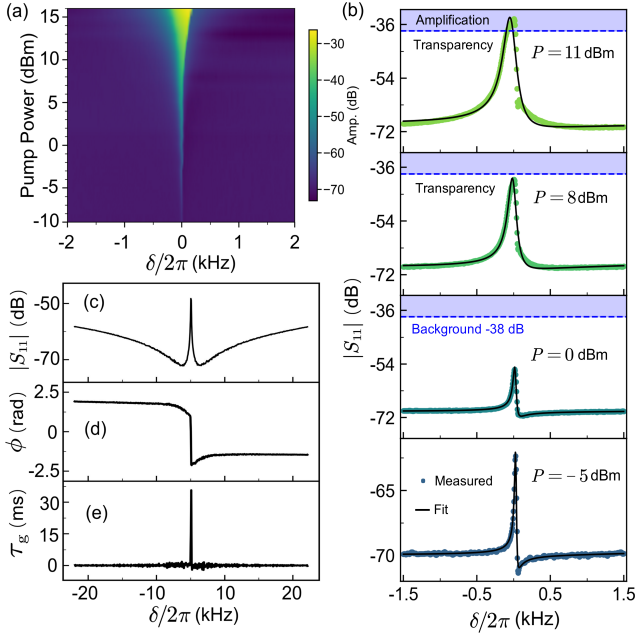


FIG. 3. (a) Reflection spectra $|S_{11}|$ of the AMIT window (color scale) as a function of red-detuned pump power. (b) Detailed view of the transition region from (a) for selected drive powers with the fitted AMIT (red lines). (c)–(e) Measured transparency window characteristics at a pump power of 3 dBm. (c) the transmission amplitude of the AMIT peak, (d) the accompanying steep phase dispersion, and (e) the resulting group delay τ_g calculated from the phase derivative.

is given by:

$$t_p(\delta) = 1 - \frac{\kappa_{\text{ex}} + \frac{|G_{\text{disp}}G_{\text{diss}}|\chi_m(\delta)\kappa_c}{2\Delta} \left(i + \frac{G_{\text{diss}}}{2G_{\text{disp}}\Delta\chi_{\text{au}}(0)} \right)}{\frac{1}{\chi_{\text{au}}(\delta)} + |G_{\text{disp}}|^2\chi_m(\delta)\left[1 + \left(\frac{G_{\text{diss}}}{2G_{\text{disp}}\Delta\chi_{\text{au}}(0)}\right)^2\right]} \quad (3)$$

where the relative probe detuning is $\delta = \omega_p - \omega_{\text{au}}$; $\chi_{\text{au}}(\delta)$ and $\chi_m(\delta)$ represent the susceptibility of the acoustical cavity and mechanical mode, respectively. Correspondingly, the effective mechanical linewidth is modified by dissipative coupling compared to the purely dispersive case and can be expressed as $\gamma_{\text{eff}} \approx \gamma_m + \frac{4|G_{\text{disp}}|^2}{\kappa} \left(1 - \left|\frac{G_{\text{diss}}\kappa_c}{2G_{\text{disp}}\Delta}\right|\right)$, explicitly demonstrating the dynamical backaction exerted by the HBAR on the SiN membrane.

The dependence of the AMIT window transmission on the pump power is shown in Fig. 3(a) and reveals a broadened linewidth and an increasing amplitude as the power increases. The zoomed-in spectra in Fig. 3(b) further reveal key signatures of dissipative coupling, including the asymmetry and a peak rising above the background baseline. The solid lines represent fits based on the theoretical model. At pump power $P = -5$ dBm, the fit yields $|G_{\text{disp}}/G_{\text{diss}}| \approx 0.2$ according to Eq. (3). Since both G_{disp} and G_{diss} scale linearly with the intracavity field amplitude \bar{a} , the ratio $|g_{\text{disp}}/g_{\text{diss}}|$ remains approximately constant at 0.8 [66]. As the pump power increases, the system enters the nonlinear regime, introducing additional coupling contributions that cause $|g_{\text{disp}}/g_{\text{diss}}|$ to

vary with the pump power. Meanwhile, dynamic backaction significantly reshapes the mechanical response. At $P = 11$ dBm, the Fano-like fitting of AMIT yields $|G_{\text{disp}}/G_{\text{diss}}| \approx 0.05$, indicating that the effective dissipative coupling strength is 20 times larger than the dispersive coupling, the highest ratio among reported hybrid dissipative-dispersive systems. This confirms the dominance of dissipative coupling under strong pumping, which is enhanced by the factor Δ/κ_c and g_{diss} . A striking manifestation of this dominance is a reflection coefficient that exceeds the background level ($|S_{11}| > -38$ dB), a feature impossible with pure dispersive coupling. Finally, the single-photon coupling strength in the linear regime obtained by fitting t_p in Fig. 3 agrees in order of magnitude with the directly measured value $g_0/2\pi \sim 10^{-2}$ Hz [66].

A hallmark of AMIT is the associated slow-acoustic effect, where the steep phase dispersion across the transparency window slows the propagation of an acoustic pulse. For probe pulses with bandwidths narrower than the effective linewidth γ_{eff} , the steep phase dispersion induces a significant group delay $\tau_g = -d\phi/d\delta$. This is demonstrated in Fig. 3(c–e): panel (c) displays the transparency window at $P=3$ dBm, panel (d) shows the corresponding phase $\phi = \arg[t_p(\delta)]$ with its steep resonant slope, and panel (e) presents the derived group delay, reaching a maximum of about 35 ms.

HBAR frequency combs via nonlinear acousto-mechanical coupling.—The observed change in the ratio $g_{\text{disp}}/g_{\text{diss}}$ indicates that the system is being driven into a regime where the interplay between dispersive and dissipative couplings is strongly power dependent. Beyond the linear regime, the radiation-pressure-type interaction gives rise to an effective Kerr nonlinearity. This is characterized by the Hamiltonian $\mathcal{H}_{\text{int}}^{\text{non}} \approx \hbar\chi\hat{a}^\dagger\hat{a}^\dagger\hat{a}\hat{a}$, where the nonlinear coefficient $\chi \propto g_0^2$ originates from the second-order mechanical correction to the cavity field energy [69, 70]. In the strong-driving regime, the large-amplitude mechanical oscillation X_m induces a periodic phase modulation on the HBAR cavity field, described by $a(t) = e^{-i\zeta\cos(\omega_m t)} \sum_n a_n e^{in\omega_m t}$. Here, $\zeta = g_0 X_m/\omega_m$ represents the nonlinear modulation depth, and a_n is the amplitude of the n -th sideband.

To harness the induced Kerr-type nonlinearity for spectral synthesis, we implement a two-tone driving scheme, as illustrated in Fig. 4(a). By separately altering the resonant driving power (P_1) and the red sideband pump power (P_2), we achieve deterministic control over the spectral span of the resulting acoustic frequency comb (AFC) [Fig. 4(b)]. In the strong drive power regime (15 dBm), a robust AFC emerges with up to 14 well-resolved teeth, characterized by a uniform spacing precisely matched to the mechanical frequency ω_m . The intensity envelope [Fig. 4(c)] and the corresponding Fourier transform [$P_2 = 15$ dBm in Fig. 4(b)] directly map the profile of the nonlinear modulation function. Crucially, the phase coherence of the generated AFC is rigorously verified through both temporal and phase-space analysis. Long-range phase coherence is corroborated by the periodic envelope of the in-phase component [Fig. 4(c)] and the stability

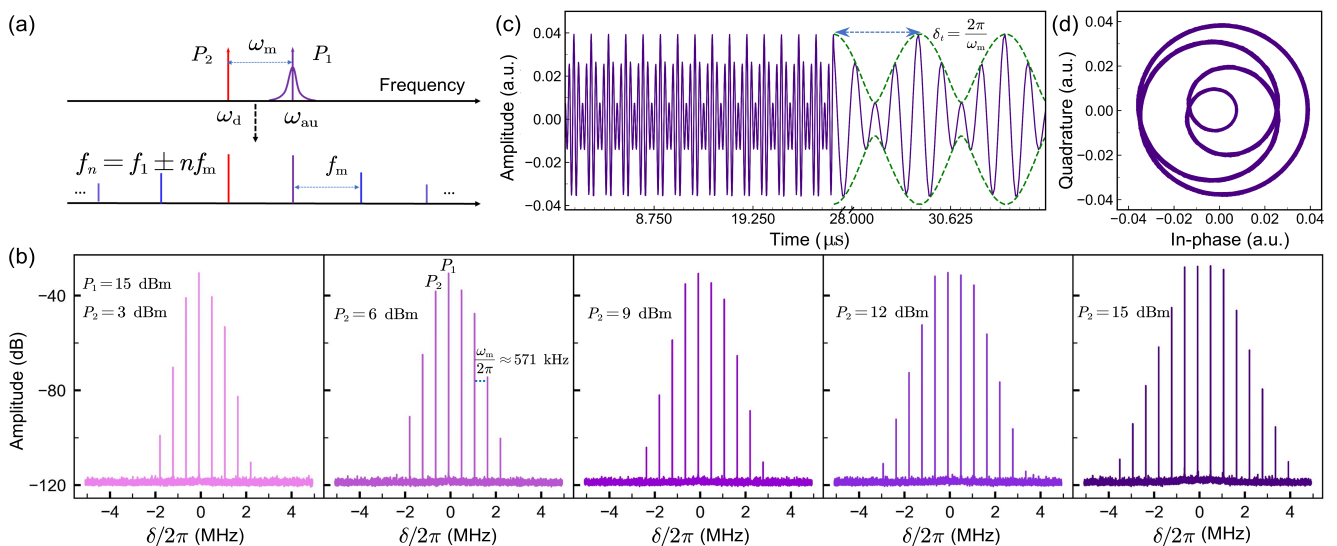


FIG. 4. (a) Schematics of the two-tone pumping configuration, consisting of a resonant drive (P_1) and a red-sideband drive (P_2 at $\Delta \approx -\omega_m$). (b) Evolution of the AFC spectra measured by RSA under varying pump powers, with $P_1 = 15$ dBm fixed and P_2 varied. Controllable tooth counts and equidistant sidebands are observed. (c) Time-domain trace of the in-phase component, exhibiting clear periodic oscillations with $\delta_t = 1.75 \mu\text{s}$. (d) Lissajous figure reconstructed from the IQ amplitudes, where the closed and stable orbits verify the long-range phase coherence of the generated frequency combs.

of the Lissajous orbits reconstructed from the time-domain IQ data [Fig. 4(d)], where the period matches the mechanical cycle $\delta_t = 2\pi/\omega_m = 1.75 \mu\text{s}$, confirming that the modulation originates from the vibration of the fundamental mechanical mode of the SiN membrane.

Conclusion.—We have proposed a hybrid acousto-mechanical platform that enables parametric coupling between high-frequency HBAR modes and low-frequency mechanical vibrations in the device, where mechanical displacement modulates the external dissipation rate of the acoustic cavity. We have achieved the highest reported ratio of dissipative and dispersive optomechanical couplings ($|G_{\text{diss}}/G_{\text{disp}}| \approx 20$) to date. The high-quality factors of the HBAR modes enable operation within the resolved-sideband regime at room temperature, as demonstrated by the observation of both acousto-mechanically induced transparency (AMIT) and amplification (AMIA) even under red-sideband pumping. Furthermore, the inherent Kerr nonlinearity of this interface enables the generation of phase-coherent acoustic frequency combs via a precise two-tone pumping scheme. Importantly, the device is inherently cryo-compatible for quantum-regime operation, yet under ambient conditions, it eliminates the need for cryogenic infrastructure, offering a paradigm shift for precision metrology and sensing as room-temperature alternatives to superconducting electromechanical systems. Furthermore, the ability to interface a dense manifold of HBAR modes with a mechanical resonator establishes robust and scalable architectures for high-capacity phononic information processing [71–73]. This versatile system opens new frontiers for exploring complex many-body dynamics, nonlinear phonon lasers, and topological transport

in large-scale acoustic networks [74–76].

Acknowledgements.—Y. L. conceived the original idea, designed and fabricated the device, and coordinated the research. X. J. performed the measurements with help of Q. L. and drafted the manuscript with input from H. S., L. W., M. A. S., and Y. L. All authors approved the final version of this work for publication. The authors acknowledge the support of the National Natural Science Foundation of China (No. 92365210, No. 12374325 and No. 12304387), Beijing Natural Science Foundation (Z240007), the National Key Research and Development Program of China (Grant No. 2022YFA1405200), European Research Council (contract 101019712), Research Council of Finland (Finnish Quantum Flagship, No. 358877) and the Young Elite Scientists Sponsorship Program by CAST (Grant No. 2023QNRC001). This work is also supported by Beijing Municipal Science and Technology Commission (Grant No. Z221100002722011).

* These authors contributed equally to this work.

† liuy1@baqis.ac.cn

‡ litf@tsinghua.edu.cn

- [1] S. Olenik, H. S. Lee, and F. Güder, The future of near-field communication-based wireless sensing, *Nat. Rev. Mater.* **6**, 286 (2021).
- [2] X. Zhao, M. Zhao, W. Peng, and Y. He, Review of bulk acoustic wave resonant optical detectors, *Sens. Actuator A-Phys.* **355**, 114333 (2023).
- [3] M. Parker, A multi-mode MEMS acoustic clock, *Nat. Electron.* **8**, 1124 (2025).
- [4] M. Goryachev, W. M. Campbell, I. S. Heng, S. Galliou, E. N.

- Ivanov, and M. E. Tobar, Rare events detected with a bulk acoustic wave high frequency gravitational wave antenna, *Phys. Rev. Lett.* **127**, 071102 (2021).
- [5] M. H. de Jong and L. Mercier de Lépinay, Complete quantum toolbox for an acoustic resonator, *Nat. Phys.* **20**, 1369 (2024).
- [6] Y. Chu, P. Kharel, W. H. Renninger, L. D. Burkhardt, L. Frunzio, P. T. Rakich, and R. J. Schoelkopf, Quantum acoustics with superconducting qubits, *Science* **358**, 199 (2017).
- [7] P. Kharel, Y. Chu, D. Mason, E. A. Kittlaus, N. T. Otterstrom, S. Gertler, and P. T. Rakich, Multimode strong coupling in cavity optomechanics, *Phys. Rev. Appl.* **18**, 024054 (2022).
- [8] V. J. Gokhale, B. P. Downey, D. S. Katzer, N. Nepal, A. C. Lang, R. M. Stroud, and D. J. Meyer, Epitaxial bulk acoustic wave resonators as highly coherent multi-phonon sources for quantum acoustodynamics, *Nat. Commun.* **11**, 2314 (2020).
- [9] U. Von Lüpke, Y. Yang, M. Bild, L. Michaud, M. Fadel, and Y. Chu, Parity measurement in the strong dispersive regime of circuit quantum acoustodynamics, *Nat. Phys.* **18**, 794 (2022).
- [10] X. Han, W. Fu, M. Xu, Y. Xu, and H. X. Tang, Superconducting cavity electromechanics: The realization of an acoustic frequency comb at microwave frequencies, *Phys. Rev. Lett.* **129**, 107701 (2022).
- [11] X. Han, C.-L. Zou, and H. X. Tang, Multimode strong coupling in superconducting cavity piezoelectromechanics, *Phys. Rev. Lett.* **117**, 123603 (2016).
- [12] Y. Yang, I. Kladarić, M. Drimmer, U. von Lüpke, D. Lentnerman, J. Bus, S. Marti, M. Fadel, and Y. Chu, A mechanical qubit, *Science* **386**, 783 (2024).
- [13] M. Bild, M. Fadel, Y. Yang, U. Von Lüpke, P. Martin, A. Bruno, and Y. Chu, Schrödinger cat states of a 16-microgram mechanical oscillator, *Science* **380**, 274 (2023).
- [14] B. Schriniski, Y. Yang, U. von Lupke, M. Bild, Y. Chu, K. Hornberger, S. Nimmrichter, and M. Fadel, Macroscopic quantum test with bulk acoustic wave resonators, *Phys. Rev. Lett.* **130**, 133604 (2023).
- [15] M.-H. Chou, E. Dumur, Y. P. Zhong, G. A. Peairs, A. Bienfait, H.-S. Chang, C. R. Conner, J. Grebel, R. G. Povey, K. J. Satzinger, and A. N. Cleland, Measurements of a quantum bulk acoustic resonator using a superconducting qubit, *Appl. Phys. Lett.* **117**, 254001 (2020).
- [16] W. Crump, A. Valimaa, and M. A. Sillanpää, Coupling high-overtone bulk acoustic wave resonators via superconducting qubits, *Appl. Phys. Lett.* **123**, 134004 (2023).
- [17] M. Kervinen, J. E. Ramírez-Muñoz, A. Välimaa, and M. A. Sillanpää, Landau-Zener-Stückelberg interference in a multimode electromechanical system in the quantum regime, *Phys. Rev. Lett.* **123**, 240401 (2019).
- [18] M. Kervinen, I. Rissanen, and M. Sillanpää, Interfacing planar superconducting qubits with high overtone bulk acoustic phonons, *Phys. Rev. B* **97**, 205443 (2018).
- [19] Q. R. Rahman, I. Kladarić, M.-E. Kern, L. Lachman, Y. Chu, R. Filip, and M. Fadel, Genuine quantum non-Gaussianity and metrological sensitivity of Fock states prepared in a mechanical resonator, *Phys. Rev. Lett.* **134**, 180801 (2025).
- [20] Y. Chu, P. Kharel, T. Yoon, L. Frunzio, P. T. Rakich, and R. J. Schoelkopf, Creation and control of multi-phonon Fock states in a bulk acoustic-wave resonator, *Nature* **563**, 666 (2018).
- [21] P. Kharel, G. I. Harris, E. A. Kittlaus, W. H. Renninger, N. T. Otterstrom, J. G. Harris, and P. T. Rakich, High-frequency cavity optomechanics using bulk acoustic phonons, *Sci. Adv.* **5**, eaav0582 (2019).
- [22] H. H. Diamandi, Y. Luo, D. Mason, T. B. Kanmaz, S. Ghosh, M. Pavlovich, T. Yoon, R. Behunin, S. Puri, J. G. Harris, *et al.*, Optomechanical control of long-lived bulk acoustic phonons in the quantum regime, *Nat. Phys.* **21**, 1482 (2025).
- [23] D. Tomasella, S. Tarrago Velez, S. B. Nielsen, J. Van der Heijden, U. B. Hoff, and U. L. Andersen, Strong optomechanical coupling at room temperature with a centimeter-scale quartz crystal, *Phys. Rev. Appl.* **23**, 054024 (2025).
- [24] W. H. Renninger, P. Kharel, R. O. Behunin, and P. T. Rakich, Bulk crystalline optomechanics, *Nat. Phys.* **14**, 601 (2018).
- [25] H. M. Doeleman, T. Schatteburg, R. Benevides, S. Vollenweider, D. Macri, and Y. Chu, Brillouin optomechanics in the quantum ground state, *Phys. Rev. Res.* **5**, 043140 (2023).
- [26] L. Fan, C.-L. Zou, R. Cheng, X. Guo, X. Han, Z. Gong, S. Wang, and H. X. Tang, Superconducting cavity electro-optics: A platform for coherent photon conversion between superconducting and photonic circuits, *Sci. Adv.* **4**, eaar4994 (2018).
- [27] R. Sahu, L. Qiu, W. Hease, G. Arnold, Y. Minoguchi, P. Rabl, and J. M. Fink, Entangling microwaves with light, *Science* **380**, 718 (2023).
- [28] W. Hease, A. Rueda, R. Sahu, M. Wulf, G. Arnold, H. G. Schwefel, and J. M. Fink, Bidirectional electro-optic wavelength conversion in the quantum ground state, *PRX Quantum* **1**, 020315 (2020).
- [29] C. Möhl, A. Riedhauser, M. Glantschnig, D. Caimi, U. Drechsler, A. Olziarsky, D. Sabonis, D. I. Indolese, T. M. Karg, and P. Seidler, Bidirectional microwave-optical conversion with an integrated soft-ferroelectric barium titanate transducer, *Phys. Rev. X* **15**, 041044 (2025).
- [30] X. Han, W. Fu, C.-L. Zou, L. Jiang, and H. X. Tang, Microwave-optical quantum frequency conversion, *Optica* **8**, 1050 (2021).
- [31] Y. Chu and S. Gröblacher, A perspective on hybrid quantum opto- and electromechanical systems, *Appl. Phys. Lett.* **117**, 150503 (2020).
- [32] S. Barzanjeh, A. Xuereb, S. Gröblacher, M. Paternostro, C. A. Regal, and E. M. Weig, Optomechanics for quantum technologies, *Nat. Phys.* **18**, 15 (2022).
- [33] X. Xi, I. Chernobrovkin, J. Kořata, M. B. Kristensen, E. Langman, A. S. Sørensen, O. Zilberberg, and A. Schliesser, A soft-clamped topological waveguide for phonons, *Nature* **642**, 947 (2025).
- [34] Y. Liu, H. Sun, Q. Liu, H. Wu, M. A. Sillanpää, and T. Li, Degeneracy-breaking and long-lived multimode microwave electromechanical systems enabled by cubic silicon-carbide membrane crystals, *Nat. Commun.* **16**, 1207 (2025).
- [35] M. B. Kristensen, N. Kralj, E. C. Langman, and A. Schliesser, Long-lived and efficient optomechanical memory for light, *Phys. Rev. Lett.* **132**, 100802 (2024).
- [36] Y. Liu, Q. Liu, H. Sun, M. Chen, S. Wang, and T. Li, Coherent memory for microwave photons based on long-lived mechanical excitations, *npj Quantum Inf.* **9**, 80 (2023).
- [37] T. Liu, F. Pagliano, R. van Veldhoven, V. Pogoretskiy, Y. Jiao, and A. Fiore, Integrated nano-optomechanical displacement sensor with ultrawide optical bandwidth, *Nat. Commun.* **11**, 2407 (2020).
- [38] Y. Liu, Q. Liu, S. Wang, Z. Chen, M. A. Sillanpää, and T. Li, Optomechanical anti-lasing with infinite group delay at a phase singularity, *Phys. Rev. Lett.* **127**, 273603 (2021).
- [39] Y. Tsaturyan, A. Barg, E. S. Polzik, and A. Schliesser, Ultracoherent nanomechanical resonators via soft clamping and dissipation dilution, *Nat. Nanotechnol.* **12**, 776 (2017).
- [40] R. A. Norte, J. P. Moura, and S. Gröblacher, Mechanical resonators for quantum optomechanics experiments at room temperature, *Phys. Rev. Lett.* **116**, 147202 (2016).
- [41] S. Chakram, Y. Patil, L. Chang, and M. Vengalattore, Dissipa-

- tion in ultrahigh quality factor SiN membrane resonators, *Phys. Rev. Lett.* **112**, 127201 (2014).
- [42] M. H. J. de Jong, A. Ganesan, A. Cupertino, S. Groblacher, and R. A. Norte, Mechanical overtone frequency combs, *Nat. Commun.* **14**, 1458 (2023).
- [43] X. Ren, J. Pan, M. Yan, J. Sheng, C. Yang, Q. Zhang, H. Ma, Z. Wen, K. Huang, H. Wu, *et al.*, Dual-comb optomechanical spectroscopy, *Nat. Commun.* **14**, 5037 (2023).
- [44] G. Huang, A. Beccari, N. J. Engelsen, and T. J. Kippenberg, Room-temperature quantum optomechanics using an ultralow noise cavity, *Nature* **626**, 512 (2024).
- [45] M. Rossi, D. Mason, J. Chen, Y. Tsaturyan, and A. Schliesser, Measurement-based quantum control of mechanical motion, *Nature* **563**, 53 (2018).
- [46] V. Fedoseev, F. Luna, I. Hedgepeth, W. Löffler, and D. Bouwmeester, Stimulated raman adiabatic passage in optomechanics, *Phys. Rev. Lett.* **126**, 113601 (2021).
- [47] R. Delaney, M. Urmeý, S. Mittal, B. Brubaker, J. Kindem, P. Burns, C. Regal, and K. Lehnert, Superconducting-qubit readout via low-backaction electro-optic transduction, *Nature* **606**, 489 (2022).
- [48] M. Mirhosseini, A. Sipahigil, M. Kalaei, and O. Painter, Superconducting qubit to optical photon transduction, *Nature* **588**, 599 (2020).
- [49] A. P. Higginbotham, P. Burns, M. Urmeý, R. Peterson, N. Kampel, B. Brubaker, G. Smith, K. Lehnert, and C. Regal, Harnessing electro-optic correlations in an efficient mechanical converter, *Nat. Phys.* **14**, 1038 (2018).
- [50] L. Shao, M. Yu, S. Maity, N. Sinclair, L. Zheng, C. Chia, A. Shams-Ansari, C. Wang, M. Zhang, K. Lai, and M. Loncar, Microwave-to-optical conversion using lithium niobate thin-film acoustic resonators, *Optica* **6**, 1498 (2019).
- [51] W. Fu, M. Xu, X. Liu, C.-L. Zou, C. Zhong, X. Han, M. Shen, Y. Xu, R. Cheng, S. Wang, L. Jiang, and H. X. Tang, Cavity electro-optic circuit for microwave-to-optical conversion in the quantum ground state, *Phys. Rev. A* **103**, 053504 (2021).
- [52] K. C. Balram, M. I. Davanco, J. D. Song, and K. Srinivasan, Coherent coupling between radiofrequency, optical and acoustic waves in piezo-optomechanical circuits, *Nat. Photon.* **10**, 346 (2016).
- [53] J. Holzgrafe, N. Sinclair, D. Zhu, A. Shams-Ansari, M. Colangelo, Y. Hu, M. Zhang, K. K. Berggren, and M. Loncar, Cavity electro-optics in thin-film lithium niobate for efficient microwave-to-optical transduction, *Optica* **7**, 1714 (2020).
- [54] H. Zhao, A. Bozkurt, and M. Mirhosseini, Electro-optic transduction in silicon via gigahertz-frequency nanomechanics, *Optica* **10**, 790 (2023).
- [55] T. Blésin, H. Tian, S. A. Bhave, and T. J. Kippenberg, Quantum coherent microwave-optical transduction using high-overtone bulk acoustic resonances, *Phys. Rev. A* **104**, 052601 (2021).
- [56] H. Tian, J. Liu, B. Dong, J. C. Skehan, M. Zervas, T. J. Kippenberg, and S. A. Bhave, Hybrid integrated photonics using bulk acoustic resonators, *Nat. Commun.* **11**, 3073 (2020).
- [57] F. Elste, S. M. Girvin, and A. A. Clerk, Quantum noise interference and backaction cooling in cavity nanomechanics, *Phys. Rev. Lett.* **102**, 207209 (2009).
- [58] A. G. Primo, N. C. Carvalho, C. M. Kersul, N. C. Frateschi, G. S. Wiederhecker, and T. P. M. Alegre, Quasinormal-mode perturbation theory for dissipative and dispersive optomechanics, *Phys. Rev. Lett.* **125**, 233601 (2020).
- [59] T. Weiss, C. Bruder, and A. Nunnenkamp, Strong-coupling effects in dissipatively coupled optomechanical systems, *New J. Phys.* **15**, 045017 (2013).
- [60] A. Bärnthaler, S. Rotter, F. Libisch, J. Burgdörfer, S. Gehler, U. Kuhl, and H.-J. Stöckmann, Probing decoherence through fano resonances, *Phys. Rev. Lett.* **105**, 056801 (2010).
- [61] M. Kazouini, J. Peter, Z. E. Guo, B. Wilde, K. Uhl, D. Koelle, R. Kleiner, and D. Bothner, Tunable and nonlinearity-enhanced dispersive-plus-dissipative coupling in photon-pressure circuits, *Nature Communications* **17**, 2789 (2026).
- [62] A. W. Barnard, M. Zhang, G. S. Wiederhecker, M. Lipson, and P. L. McEuen, Real-time vibrations of a carbon nanotube, *Nature* **566**, 89 (2019).
- [63] S. Basiri-Esfahani, A. Armin, S. Forstner, and W. P. Bowen, Precision ultrasound sensing on a chip, *Nat. Commun.* **10**, 132 (2019).
- [64] A. Karpenko and S. P. Vyatchanin, Dissipative coupling, dispersive coupling, and their combination in cavityless optomechanical systems, *Phys. Rev. A* **102**, 023513 (2020).
- [65] A. G. Primo, P. V. Pinho, R. Benevides, S. Groblacher, G. S. Wiederhecker, and T. P. M. Alegre, Dissipative optomechanics in high-frequency nanomechanical resonators, *Nat. Commun.* **14**, 5793 (2023).
- [66] See Supplemental Material for the details of experimental setup and device characteristics, derivation of acousto-mechanical coupling, AMIT and AMIA, and HBAR combs.
- [67] J. S. Jin, Mechanical vibration-induced suppression of transverse acoustic phonons in silicon due to Akhiezer damping, *AIP Adv.* **14**, 105332 (2024).
- [68] J. Groenen, F. Poinssotte, A. Zwick, C. Sotomayor Torres, M. Prunnila, and J. Ahopelto, Inelastic light scattering by longitudinal acoustic phonons in thin silicon layers: From membranes to silicon-on-insulator structures, *Phys. Rev. B* **77**, 045420 (2008).
- [69] S. Wu, Y. Liu, Q. Liu, S.-P. Wang, Z. Chen, and T. Li, Hybridized frequency combs in multimode cavity electromechanical system, *Phys. Rev. Lett.* **128**, 153901 (2022).
- [70] Y. Wang, M. Zhang, Z. Shen, G.-T. Xu, R. Niu, F.-W. Sun, G.-C. Guo, and C.-H. Dong, Optomechanical frequency comb based on multiple nonlinear dynamics, *Phys. Rev. Lett.* **132**, 163603 (2024).
- [71] M. Merklein, B. Stiller, K. Vu, S. J. Madden, and B. J. Eggleton, A chip-integrated coherent photonic-phononic memory, *Nat. Commun.* **8**, 574 (2017).
- [72] J. C. Taylor, E. Chatterjee, W. F. Kindel, D. Soh, and M. Eichenfield, Reconfigurable quantum phononic circuits via piezo-acoustomechanical interactions, *npj Quantum Inf.* **8**, 19 (2022).
- [73] L. Zhang, C. Cui, Y. Xue, P. Chen, and L. Fan, Scalable photonic-phononic integrated circuitry for reconfigurable signal processing, *Nat. Commun.* **16**, 2718 (2025).
- [74] D. Yao, L. Ye, Z. Fu, Q. Wang, H. He, J. Lu, W. Deng, X. Huang, M. Ke, and Z. Liu, Topological network modes in a twisted Moiré phononic crystal, *Phys. Rev. Lett.* **132**, 266602 (2024).
- [75] Y. He, T. Kuang, X. Han, Z. Feng, X. Chen, W. Xiong, S. Jin, Z. Tan, Q. Zhang, H. Luo, H. Jing, and G. Xiao, Coherent acoustic frequency comb via Floquet engineering of optical tweezer phonon lasers, *Sci. Adv.* **11**, eadv9984 (2025).
- [76] X.-B. Xu, M. Oudich, Y. Zeng, J.-Z. Zhang, Y.-H. Yang, J.-Q. Wang, W. Wang, L. Sun, G.-C. Guo, Y. Jing, *et al.*, Gigahertz topological phononic circuits based on micrometre-scale unsuspended waveguide arrays, *Nat. Electron.* **8**, 689 (2025).